

Noise2Inverse: Self-supervised deep convolutional denoising for linear inverse problems in imaging

Allard A. Hendriksen, Daniël M. Pelt, K. Joost Batenburg ^{*†}

February 3, 2020

Abstract

Recovering a high-quality image from noisy indirect measurement is an important problem with many applications. For such inverse problems, supervised deep convolutional neural network (CNN)-based denoising methods have shown strong results, but their success critically depends on the availability of a high-quality training dataset of similar measurements. For image denoising, methods are available that enable training without a separate training dataset by assuming that the noise in two different pixels is uncorrelated. However, this assumption does not hold for inverse problems, resulting in artifacts in the output of existing methods. Here, we propose Noise2Inverse, a deep CNN-based denoising method for linear inverse problems in imaging that does not require any additional clean or noisy data. Training a CNN-based denoiser is enabled by exploiting the noise model to compute multiple statistically independent reconstructions. We develop a theoretical framework which shows that such training indeed obtains a denoising CNN, assuming the measured noise is element-wise independent and zero-mean. On simulated CT datasets, Noise2Inverse demonstrates a substantial improvement in peak signal-to-noise ratio ($> 2\text{dB}$) and structural similarity index ($> 30\%$) compared to image denoising methods and conventional reconstruction methods, such as Total-Variation Minimization. We also demonstrate that the method is able to significantly reduce noise in challenging real-world experimental datasets.

^{*}A. A. Hendriksen, D. M. Pelt, and K. J. Batenburg are with the Centrum Wiskunde & Informatica.

[†]K. J. Batenburg is with the Leiden Institute of Advanced Computer Science.

1 Introduction

The inverse problem of recovering an image from an indirect measurement occurs in a variety of scientific fields and industrial applications, such as computed tomography (CT) [1], magnetic resonance imaging (MRI) [2], and geophysical modeling [3]. Statistical phenomena introduce noise into the indirect measurement, which cause errors in the reconstructed image. Controlling this error, i.e., *denoising*, is a central problem in these inverse problems in imaging [4–10].

Deep convolutional neural network (CNN)-based methods are able to accurately denoise reconstructed images in several inverse problems [4–8]. These networks are trained in a *supervised* setting, which amounts to finding the network parameters that best compute a mapping from noisy to clean reconstructed images on a dataset of example image pairs. However, the success of these deep learning methods critically depends on the availability of such a high-quality training dataset of similar images [4].

For photographic image denoising, recent work has shown that deep learning may be possible without obtaining high quality target images, by instead training on paired noisy images [11, 12]. Nonetheless, such *Noise2Noise* training still requires additional noisy data. The feasibility of image denoising by *self-supervised* training, that is, training with *single* instead of paired noisy images, was demonstrated by [13, 14]. These self-supervised training methods, such as Noise2Self, depend on the assumption that noise in one pixel is statistically independent from noise in another pixel.

In inverse problems, reconstructed images may exhibit coupling of the measured noise [5]. In CT, for instance, back-projection smears out the noise

in a detector pixel across a line through the reconstructed image. Naturally, this causes the noise in one pixel to be statistically dependent on noise in other pixels of the reconstructed image.

In this paper, we demonstrate that a straightforward application of Noise2Self to reconstructed CT images delivers substantially inferior results compared to results obtained on photographic images, for which it was developed. We analyze the cause of this apparent mismatch, and propose Noise2Inverse, a new approach that is specifically designed for linear inverse problems in imaging to overcome these limitations.

In the proposed Noise2Inverse approach, the training regime explicitly takes into account the structure of the noise in the inverse problem. Specifically, we exploit the properties of the physical forward model to compute multiple statistically independent instances of the reconstruction. This permits training a CNN to remove the noise from the reconstruction. We stress that our method can be applied to existing datasets without acquiring additional data.

In recent work [10], a similar approach was developed specifically for Cryo-transmission electron microscopy. In contrast, we embed our method in a theoretical framework for generic linear inverse problem in imaging, and perform an extensive hyper-parameter study.

Specifically, in this paper, we perform a qualitative and quantitative comparison to conventional iterative reconstruction and self-supervised deep image denoising techniques. We evaluate these methods on several simulated low-dose CT datasets. We include results on an existing experimentally acquired CT dataset, for which no low-noise data is available. The effectiveness of our method is explained through a theoretical framework that provides additional guidance and insight on the properties of the general approach. In addition, we present a systematic analysis of the hyper-parameters of the proposed method.

This paper is structured as follows. In Section 2, we introduce linear inverse problems and deep learning for image denoising, including self-supervised methods. In Section 3, we introduce the proposed Noise2Inverse method, and show its theoretical properties, which we use to develop an implementation for computed tomography. In Section 4, we perform experiments to compare the perfor-

mance of Noise2Inverse, conventional reconstruction techniques, and Noise2Self-based methods on real and simulated CT datasets. In addition, we perform a hyper-parameter study of the proposed method. We discuss these results in Section 5, and conclude in Section 6.

2 Notation and concepts

As prerequisites for describing our Noise2Inverse approach, we first discuss deep learning methods for image denoising, including strategies for training neural networks when clean images are unavailable. In addition, we review linear inverse problems, where we discuss that denoising reconstructed images introduces additional difficulties.

2.1 Deep learning for image denoising

The goal of image denoising is to recover a 2D image $\mathbf{y} \in \mathcal{Y} = \mathbb{R}^m$ from a measurement $\tilde{\mathbf{y}} \in \mathcal{Y}$ that is corrupted by random noise ϵ , taking values in \mathcal{Y} . This problem is described by the equation

$$\tilde{\mathbf{y}} = \mathbf{y} + \epsilon. \quad (1)$$

It is common to assume that the entries of the noise vector ϵ are mutually independent. Many image denoising methods rely on this assumption [13,15,16]. In addition, these methods assume that the image exhibits some statistically meaningful structure that can be exploited to remove the noise. The popular BM3D algorithm [16], for example, exploits non-local self-similarity, i.e., the expectation that certain structures of the image are repeated elsewhere in the image.

Instead of relying on an explicit image prior, prior knowledge can be based on a range of example images, as is done in deep learning. In particular, deep convolutional neural networks (CNNs) have been recognized as a powerful and versatile denoising technique [15]. We briefly introduce three training schemes for denoising with CNNs: supervised [15], Noise2Noise [12], and Noise2Self [14].

The **supervised** training scheme has access to a *training dataset* containing pairs of noisy *input* and clean *target* images

$$(\tilde{y}_i, y_i) \sim (y + \epsilon, y), \quad i = 1, \dots, N, \quad (2)$$

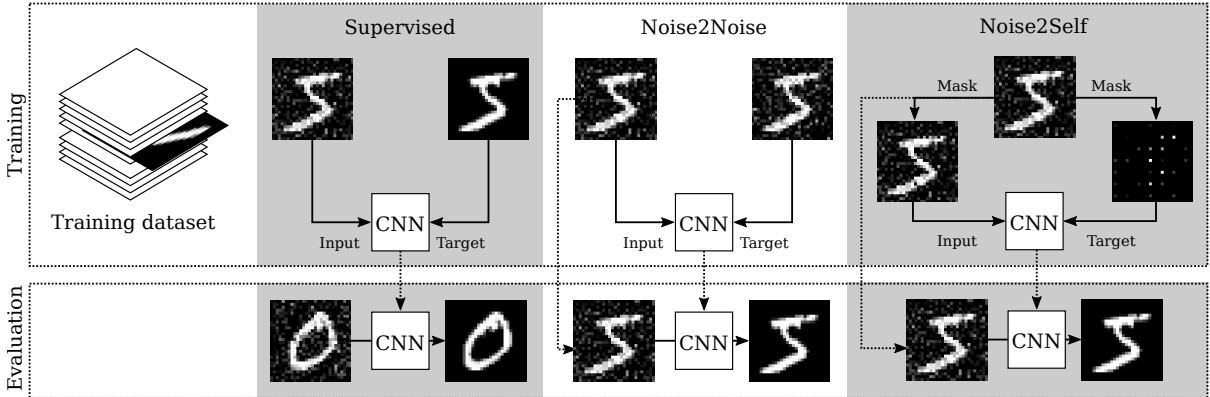


Figure 1: Three training regimes for CNN-based image denoising. Supervised training is performed with noisy and clean images, and the trained CNN is applied to unseen noisy data. Noise2Noise training is performed with pairs of noisy images. Noise2Self training is performed with just noisy images, which are split into input-target pairs. The loss is only computed where target pixels are non-zero. For Noise2Noise and Noise2Self, the trained CNN can be applied to the training data to obtain clean images.

where y is a random variable taking values in \mathcal{Y} that represents the clean images. The supervised training objective is to find a function $h^* : \mathcal{Y} \rightarrow \mathcal{Y}$,

$$h^* = \arg \min_h \mathbb{E}_{y, \epsilon} \left[\|h(y + \epsilon) - y\|_2^2 \right], \quad (3)$$

that minimizes the expected pixel-wise mean square error over the space of all possible noisy and clean images.

Solving Equation (3) is usually intractable. Therefore, the expectation is estimated by the sample mean over the training dataset, which is minimized over neural networks $f_\varphi : \mathcal{Y} \rightarrow \mathcal{Y}$ with parameters φ . The training task is then to find the optimal parameters

$$\hat{\varphi} = \arg \min_\varphi \sum_{i=1}^N \|f_\varphi(\tilde{y}_i) - y_i\|_2^2, \quad (4)$$

which minimize the loss on the sampled image pairs. The trained network $f_{\hat{\varphi}}$ is applied to unseen noisy images to obtain denoised images, as displayed in Figure 1.

In theory, the conditional expectation

$$h^*(\tilde{y}) = \mathbb{E}[y \mid y + \epsilon = \tilde{y}] \quad (5)$$

minimizes the training objective (3). In practice, the trained neural network $f_{\hat{\varphi}}$ does not equal h^* and only an approximation is obtained.

Noise2Noise training may be applied if no clean images are available, but one can measure *independent* instances of the noise for each image. The training dataset contains pairs of independent noisy images

$$(y_i + \epsilon_i, y_i + \delta_i) \sim (y + \epsilon, y + \delta), \quad i = 1, \dots, N, \quad (6)$$

where the noise δ is a random variable that is statistically independent of ϵ . The training task is to determine

$$\hat{\varphi} = \arg \min_\varphi \sum_{i=1}^N \|f_\varphi(y_i + \epsilon_i) - (y_i + \delta_i)\|_2^2, \quad (7)$$

and the trained neural network $f_{\hat{\varphi}}$ approximates

$$h^* = \arg \min_h \mathbb{E}_{y, \epsilon, \delta} \left[\|h(y + \epsilon) - (y + \delta)\|_2^2 \right]. \quad (8)$$

In theory, if the noise δ is mean-zero, i.e., $\mathbb{E}[\delta] = 0$, Equation (8) is minimized by the same function h^* as in the supervised regime (Equation (5)). In practice, Noise2Noise and supervised training indeed yield trained networks with similar denoising performance.

Noise2Self enables training a neural network denoiser without any additional images. The training dataset contains only noisy images

$$\tilde{y}_i \sim y + \epsilon, \quad i = 1, \dots, N. \quad (9)$$

The method depends on the assumption that the noise is element-wise statistically independent and mean-zero, and that the clean images exhibit some spatial correlation.

Noise2Self training uses a masking scheme that ensures that the loss compares two statistically independent images. For simplicity, we describe a simplified version of Noise2Self training, and refer to [14] for a more in-depth explanation. In each training step, the noisy image is partitioned into two images: one image — the target — contains non-adjacent pixels and the other image — the input — contains the remaining pixels. The network is trained to predict the value of a noisy pixel from its surrounding noisy pixels.

The division of pixels between the input and target image is determined by a partition \mathcal{J} of the pixels such that adjacent pixels are in different subsets. For each $J \in \mathcal{J}$, the network is trained to predict the target pixel intensities of \tilde{y}_i at locations J from an input image $\mathbb{1}_{J^C} \tilde{y}_i$ where these pixels have been masked. Here, J^C denotes the set complement of J , containing all pixel locations not contained in J , and $\mathbb{1}_J$ denotes the indicator function such that element-wise multiplication of $\mathbb{1}_J$ with an image retains pixel values in J and sets pixels to zero elsewhere. The training task is to determine

$$\hat{\varphi} = \arg \min_{\varphi} \sum_{i=1}^N \sum_{J \in \mathcal{J}} \|\mathbb{1}_J f_{\varphi}(\mathbb{1}_{J^C} \tilde{y}_i) - \mathbb{1}_J \tilde{y}_i\|_2^2. \quad (10)$$

The masking $\mathbb{1}_J$ ensures that the loss is only computed on a region J of the image that the network is trained to predict.

The inference step is performed by a function $g_{\hat{\varphi}} : \mathcal{Y} \rightarrow \mathcal{Y}$,

$$g_{\hat{\varphi}}(\tilde{y}) := \sum_{J \in \mathcal{J}} \mathbb{1}_J f_{\hat{\varphi}}(\mathbb{1}_{J^C} \tilde{y}), \quad (11)$$

that computes each output region J by applying $f_{\hat{\varphi}}$ to the image where the region J is set to zero. The function $g_{\hat{\varphi}}$ is an approximation of the function

$$g^*(\tilde{y}) = \sum_{J \in \mathcal{J}} \mathbb{1}_J \mathbb{E}[\mathbb{1}_J y \mid \mathbb{1}_{J^C} (y + \epsilon) = \mathbb{1}_{J^C} \tilde{y}]. \quad (12)$$

The function g^* computes the conditional expectation of the clean data $\mathbb{1}_J y$ given the surrounding noisy pixels. This equation explains why the Noise2Self method requires spatial correlation of

the clean images: if there were no correlation, then no information can be gained from the surrounding pixels J^C to fill in the pixels in J .

Although aforementioned methods can produce accurately denoised photographic images in many cases [12, 14, 15], a subclass of these algorithms — Noise2Self in particular — has strong requirements on the element-wise independence of the noise. These requirements do not generally hold for solutions of linear inverse problems, as we discuss next.

2.2 Linear inverse problems

We are concerned with inverse problems that are described by the equation

$$\mathbf{A}\mathbf{x} = \mathbf{y}, \quad (13)$$

where $\mathbf{x} \in \mathcal{X} = \mathbb{R}^n$ denotes an unknown image that we wish to recover, and $\mathbf{y} \in \mathcal{Y} = \mathbb{R}^m$ denotes the indirect measurement. The linear forward operator $\mathbf{A} : \mathbb{R}^n \rightarrow \mathbb{R}^m$ describes the physical model by which the measurement arises from the image \mathbf{x} . As in the image denoising setting, these measurements are corrupted by element-wise independent noise ϵ , and we write

$$\tilde{\mathbf{y}} = \mathbf{A}\mathbf{x} + \epsilon. \quad (14)$$

Reconstruction algorithms approximate the image \mathbf{x} from measured data \mathbf{y} . A subclass of these reconstruction algorithms computes a linear operator $\mathbf{R} : \mathcal{Y} \rightarrow \mathcal{X}$. Examples of linear reconstruction algorithms include the filtered backprojection algorithm for tomography and Fourier inversion for MRI [1, 2]. We denote the reconstruction from a noisy measurement by

$$\tilde{\mathbf{x}} = \mathbf{R}\tilde{\mathbf{y}} = \mathbf{R}\mathbf{y} + \mathbf{R}\epsilon. \quad (15)$$

The reconstruction operator \mathbf{R} may cause elements of the reconstructed noise $\mathbf{R}\epsilon$ to be statistically coupled, even if ϵ is element-wise independent [5]. That $\mathbf{R}\epsilon$ does not satisfy the element-wise independence property is unavoidable for all but the most trivial cases, since inverse problems are essentially defined by the intricate coupling of the unknown image with its indirect measurement.

This coupling of the noise seriously degrades the effectiveness of the Noise2Self approach, as we will

see in Section 4.3. In the next section, we propose a self-supervised method that does take into account the properties of noise in inverse problems.

3 Noise2Inverse

Suppose that we wish to examine several unknown images $\mathbf{x}_1, \dots, \mathbf{x}_N \sim \mathbf{x}$, sampled from some random variable \mathbf{x} . We obtain noisy indirect measurements

$$\tilde{\mathbf{y}}_i \sim \mathbf{A}\mathbf{x}_i + \epsilon, \quad i = 1, \dots, N, \quad (16)$$

where we assume that the noise ϵ is element-wise independent and mean-zero conditional on the data, i.e.,

$$\mathbb{E}_{\mathbf{x}, \epsilon} [\mathbf{A}\mathbf{x} + \epsilon \mid \mathbf{A}\mathbf{x} = \mathbf{y}] = \mathbf{y}. \quad (17)$$

Write $\mathbf{y}_i = \mathbf{A}\mathbf{x}_i, i = 1, \dots, N$. Our goal is to recover the clean reconstructions $\mathbf{x}_i^* = \mathbf{R}\mathbf{y}_i$, that would have been obtained in the absence of noise.

One approach is to compute noisy reconstructions, and use Noise2Self to remove the noise in the reconstructed images. Given the reconstructions of the noisy measurements $\tilde{\mathbf{x}}_i = \mathbf{R}\tilde{\mathbf{y}}_i, i = 1, \dots, N$, the training task is to determine

$$\hat{\varphi} = \arg \min_{\varphi} \sum_{J \in \mathcal{J}_x} \|\mathbb{1}_J f_{\varphi}(\mathbb{1}_{J^c} \tilde{\mathbf{x}}_i) - \mathbb{1}_J \tilde{\mathbf{x}}_i\|_2^2, \quad (18)$$

where \mathcal{J}_x is a partition of the pixels of the reconstructed images. As discussed before, however, the noise in the pixels of the different subsets $J \in \mathcal{J}_x$ are unlikely to be statistically independent.

The key idea of the proposed Noise2Inverse method is that it partitions the data in the measurement domain — where the noise is element-wise independent — but trains the CNN in the reconstruction domain. In each training step, the measured data is partitioned into an input and target component, and a neural network is trained to predict the reconstruction of one from the reconstruction of the other. After training, the neural network is applied to denoise the reconstructions.

The division of measured data between input and target is determined by a collection \mathcal{J} of sets $J \subset \{1, 2, \dots, m\}$ that represent potentially overlapping subsets of the dimensions of $\mathcal{Y} = \mathbb{R}^m$. For $J \in \mathcal{J}$, the measurement $\tilde{\mathbf{y}}_i$ is partitioned into complementary sub-measurements $\tilde{\mathbf{y}}_{i,J} \in \mathcal{Y}_J$ and

$\tilde{\mathbf{y}}_{i,J^c} \in \mathcal{Y}_{J^c}$, where J^c denotes the set complement of J with respect to $\{1, 2, \dots, m\}$.

The input and target are computed by linear reconstruction operators $\mathbf{R}_J : \mathcal{Y}_J \rightarrow \mathcal{X}$ that take into account only the measurements indicated by $J \in \mathcal{J}$. We define

$$\tilde{\mathbf{x}}_{i,J^c} = \mathbf{R}_{J^c} \tilde{\mathbf{y}}_{i,J^c} \text{ and } \tilde{\mathbf{x}}_{i,J} = \mathbf{R}_J \tilde{\mathbf{y}}_{i,J}$$

to be the input and target sub-reconstructions of $\tilde{\mathbf{y}}_i$, respectively.

The training task is to determine the parameters

$$\hat{\varphi} = \arg \min_{\varphi} \frac{1}{|\mathcal{J}|} \sum_{J \in \mathcal{J}} \sum_{i=1}^N \|f_{\varphi}(\tilde{\mathbf{x}}_{i,J^c}) - \tilde{\mathbf{x}}_{i,J}\|_2^2, \quad (19)$$

that best enable the network $f_{\hat{\varphi}}$ to predict the sub-reconstruction $\tilde{\mathbf{x}}_{i,J}$ from its complement $\tilde{\mathbf{x}}_{i,J^c}$.

For evaluation, the trained network $f_{\hat{\varphi}}$ is applied to the arrangements of the input sub-reconstructions, of which the average is computed. Write $\tilde{\mathbf{x}}_{J^c} = \mathbf{R}_{J^c} \tilde{\mathbf{y}}_{J^c}$, then the output is computed by $g_{\hat{\varphi}} : \mathcal{Y} \rightarrow \mathcal{X}$, defined by

$$g_{\hat{\varphi}}(\tilde{\mathbf{y}}) = \frac{1}{|\mathcal{J}|} \sum_{J \in \mathcal{J}} f_{\hat{\varphi}}(\tilde{\mathbf{x}}_{J^c}). \quad (20)$$

In the next section, we show why the final result $g_{\hat{\varphi}}(\tilde{\mathbf{y}}_i)$ approximates the clean reconstruction \mathbf{x}_i^* .

3.1 Theoretical framework

In this section, we embed Noise2Inverse in a theoretical framework that explains why it is an accurate denoising method. In addition, we describe design considerations that enable it to operate successfully.

Below, we show that Noise2Inverse recovers an average clean reconstruction in theory. This result is founded upon Proposition 1, which shows that functions that minimize the training loss in Equation (19) also minimize the loss with respect to the unknown clean reconstruction. Because of this behavior, the global minimum predicts a clean sub-reconstruction when given a noisy sub-reconstruction, as shown in Equation (24).

We begin by representing the clean and noisy measurements by the random variables $\mathbf{y} = \mathbf{A}\mathbf{x}$ and $\tilde{\mathbf{y}} = \mathbf{y} + \epsilon$, and define the input and target random variables by $\tilde{\mathbf{x}}_{J^c} = \mathbf{R}_{J^c} \tilde{\mathbf{y}}_{J^c}$ and $\tilde{\mathbf{x}}_J = \mathbf{R}_J \tilde{\mathbf{y}}_J$ for

$J \in \mathcal{J}$. In this case, the trained network $f_{\hat{\varphi}}$ obtained in Equation (19) approximates the function

$$h^* = \arg \min_h \frac{1}{|\mathcal{J}|} \sum_{J \in \mathcal{J}} \mathbb{E}_{\mathbf{x}, \epsilon} \|h(\tilde{\mathbf{x}}_{J^c}) - \tilde{\mathbf{x}}_J\|^2, \quad (21)$$

which minimizes the expected prediction error. We replace the subset J by a random variable \mathbf{J} taking values uniformly at random in \mathcal{J} . We define the random sub-reconstructions $\tilde{\mathbf{x}}_{J^c} = \mathbf{R}_{J^c} \tilde{\mathbf{y}}_{J^c}$ and $\tilde{\mathbf{x}}_J = \mathbf{R}_J \tilde{\mathbf{y}}_J$. The prediction error then becomes

$$\frac{1}{|\mathcal{J}|} \sum_{J \in \mathcal{J}} \mathbb{E}_{\mathbf{x}, \epsilon} \|h(\tilde{\mathbf{x}}_{J^c}) - \tilde{\mathbf{x}}_J\|^2 = \mathbb{E}_{\mu} \|h(\tilde{\mathbf{x}}_{J^c}) - \tilde{\mathbf{x}}_J\|^2,$$

where we replace the average over $J \in \mathcal{J}$ by the expectation with respect to \mathbf{J} . We denote with μ the joint measure of \mathbf{x}, ϵ , and \mathbf{J} . Define the sub-reconstruction of the clean measurement

$$\mathbf{x}^*_{\mathbf{J}} = \mathbf{R}_J \mathbf{y}_J, \quad (22)$$

which describes the reconstruction in the absence of noise. Now the expected prediction error can be decomposed into two parts.

Proposition 1. *Let $\tilde{\mathbf{x}}_J, \tilde{\mathbf{x}}_{J^c}, \mathbf{x}^*_{\mathbf{J}}$, and μ be as above. Let ϵ be element-wise independent and satisfy (17). Let \mathbf{R}_J be linear for all $J \in \mathcal{J}$. Then, for any measurable function $h : \mathcal{X} \rightarrow \mathcal{X}$, we have*

$$\mathbb{E}_{\mu} \|h(\tilde{\mathbf{x}}_{J^c}) - \tilde{\mathbf{x}}_J\|_2^2 = \mathbb{E}_{\mu} \|h(\tilde{\mathbf{x}}_{J^c}) - \mathbf{x}^*_{\mathbf{J}}\|_2^2 + \mathbb{E}_{\mu} \|\mathbf{x}^*_{\mathbf{J}} - \tilde{\mathbf{x}}_J\|_2^2. \quad (23)$$

Proposition 1 states that the self-supervised loss can be decomposed into the supervised loss, which depends on the choice of h , and the variance of the reconstruction noise, which does not depend on h . Therefore, when minimizing (23), the function h minimizes the difference between its output and the unknown clean complementary sub-reconstruction.

The loss with respect to the clean complementary sub-reconstruction, $\mathbb{E}_{\mu} \|h(\tilde{\mathbf{x}}_{J^c}) - \mathbf{x}^*_{\mathbf{J}}\|_2^2$, is minimized [17] by the function $h^* : \mathcal{X} \rightarrow \mathcal{X}$,

$$h^*(\tilde{\mathbf{x}}) = \mathbb{E}_{\mu} [\mathbf{x}^*_{\mathbf{J}} \mid \tilde{\mathbf{x}}_{J^c} = \tilde{\mathbf{x}}]. \quad (24)$$

Write $\tilde{\mathbf{x}}_{J^c} = \mathbf{R}_{J^c} \tilde{\mathbf{y}}_{J^c}$ for $J \in \mathcal{J}$. Then the output is computed by $g^* : \mathcal{Y} \rightarrow \mathcal{X}$, defined by

$$g^*(\tilde{\mathbf{y}}) = \frac{1}{|\mathcal{J}|} \sum_{J \in \mathcal{J}} \mathbb{E}_{\mu} [\mathbf{x}^*_{\mathbf{J}} \mid \tilde{\mathbf{x}}_{J^c} = \tilde{\mathbf{x}}_{J^c}]. \quad (25)$$

A noisy sub-reconstruction $\tilde{\mathbf{x}}_{J^c}$ can be explained by different values of the clean reconstruction \mathbf{x}^* . The expectation $\mathbb{E}_{\mu} [\mathbf{x}^*_{\mathbf{J}} \mid \tilde{\mathbf{x}}_{J^c} = \tilde{\mathbf{x}}_{J^c}]$ is the mean of noiseless reconstructed images consistent with the observed noisy reconstruction $\tilde{\mathbf{x}}_{J^c}$. Equation (25) therefore predicts that our method produces denoised images. In fact, it shows that the output is the mean over all clean sub-reconstructions indicated by $J \in \mathcal{J}$.

Equation (25) explains how to choose subsets \mathcal{J} . First of all, the mean of the clean sub-reconstructions $1/|\mathcal{J}| \sum_{J \in \mathcal{J}} \mathbf{x}^*_{\mathbf{J}}$ must resemble the desired clean image. This can be achieved by choosing \mathcal{J} to be a partition of $\{1, \dots, m\}$, or, by choosing \mathcal{J} such that each measured data point is contained in the same number of overlapping subsets $J \in \mathcal{J}$. Not doing so introduces a systematic bias into the reconstruction.

Second, the sub-reconstructions should be homogeneously informative throughout the image. If the sub-reconstructions are very different, or contain limited information about large parts of the image, then many dissimilar clean images are consistent with the observed noisy reconstruction, and the average over all these images will become blurred.

We note that \mathbf{x}^* denotes the clean reconstruction, rather than the unknown image. This has two consequences. First, if reconstruction artifacts arise in the absence of noise, these artifacts are preserved by our method. Second, if the reconstruction method also performs denoising operations, for instance by blurring, then the result of our method might become blurred. In the next section, we use the requirements given above to devise an approach for a specific linear inverse problem: computed tomography.

3.2 Noise2Inverse for computed tomography

In this section, we describe our implementation of Noise2Inverse for 3D parallel-beam tomography, and discuss how the implementation relates to the theoretical considerations discussed before.

The 3D parallel-beam tomography problem may be considered as a stack of 2D parallel-beam problems. In 2D parallel-beam tomography, a parallel X-ray beam penetrates an object, after which it is measured on a line detector. The line detector rotates around the object while capturing the inten-

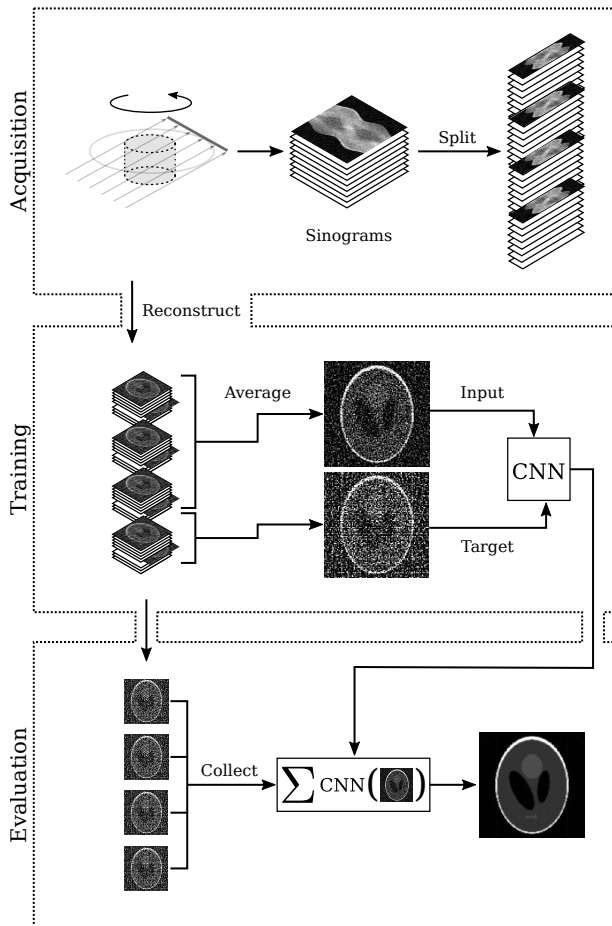


Figure 2: Noise2Inverse for computed tomography. First, 3D parallel-beam tomography obtains a stack of noisy sinograms by integrating over parallel lines at several angles. Next, the stack of sinograms is split along the angular axis. Then, the split sinograms are reconstructed to act as training dataset. During training, a dynamic subset of slices is averaged to form the input; the target is the average of the remaining slices. To obtain a low-noise result, the trained CNN is applied to all arrangements of input slices and averaged.

sity of the attenuated X-ray beam, as illustrated in the top panel of Figure 2.

In practice, a finite number of N_θ projections are acquired on a line grid of N_p detector elements at fixed angular intervals. Hence, the projection data can be described by a vector $\tilde{\mathbf{y}} \in \mathcal{Y} = \mathbb{R}^m$, $m = N_\theta \times N_p$, which is known as the *sinogram*. Likewise, the two-dimensional imaged object is represented by a vector $\mathbf{x} \in \mathcal{X} = \mathbb{R}^n$, $n = N_x^2$. We can formulate 2D parallel-beam tomography as a discrete linear inverse problem, where $\mathbf{A} = (a_{ij})$ is an $m \times n$ matrix such that a_{ij} represents the contribution of object pixel j to detector pixel i . In 3D tomography, a sequence of 2D projection images of the 3D structure is acquired, which may be converted to a stack of 2D sinograms.

The imaged object can be recovered from the sinogram by a reconstruction algorithm, such as the filtered back-projection algorithm (FBP) [1]. FBP is an example of a linear operator that couples the measured noise in the reconstruction, as described in Equation (15). In addition, it is typically fast to compute, although its reconstructions tend to be noisy [9].

The Noise2Inverse method is well-suited to denoise this kind of problem. Suppose we have obtained a stack of 2D noisy sinograms $\tilde{\mathbf{y}}_1, \tilde{\mathbf{y}}_2, \dots, \tilde{\mathbf{y}}_N$, acquired from a range of N_θ equally-spaced angles $\theta_1, \theta_2, \dots, \theta_{N_\theta}$. Our approach follows the following steps.

First, we split each sinogram $\tilde{\mathbf{y}}_i$ into K sub-sinograms $\tilde{\mathbf{y}}_{i,1}, \dots, \tilde{\mathbf{y}}_{i,K}$ such that each sub-sinogram $\tilde{\mathbf{y}}_{i,j}$ contains pixels from every K th angle $\theta_j, \theta_{j+K}, \theta_{j+2K}, \dots, \theta_{j+N_\theta-K}$. The number of splits K is a hyper-parameter of the method.

Using the FBP algorithm, we compute sub-reconstructions

$$\tilde{\mathbf{x}}_{i,j} = \mathbf{R}_j(\tilde{\mathbf{y}}_{i,j}), \quad j = 1, \dots, K. \quad (26)$$

For training, the division of the sub-reconstructions over the input and target is determined by a collection \mathcal{J} , which contains subsets $J \subset \{1, \dots, K\}$. For $J \subset \{1, \dots, K\}$, we define the mean sub-reconstruction as

$$\tilde{\mathbf{x}}_{i,J} = \frac{1}{|J|} \sum_{j \in J} \tilde{\mathbf{x}}_{i,j}. \quad (27)$$

As before, training of the neural network f_φ aims

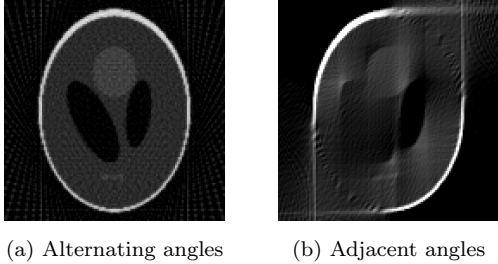


Figure 3: Two sub-reconstructions computed from a sinogram containing 92 projection angles. On the left, the image is reconstructed from 46 alternating angles. On the right, the image is reconstructed from the first 46 adjacent angles.

to find

$$\hat{\varphi} = \arg \min_{\varphi} \sum_{i=1}^N \sum_{J \in \mathcal{J}} \|f_{\varphi}(\tilde{x}_{i,J^c}) - \tilde{x}_{i,j}\|_2^2. \quad (28)$$

In this paper, we identify two training strategies specifying \mathcal{J} :

X:1 Using this strategy, the input is the mean of $K - 1$ sub-reconstructions, and the target is the remaining sub-reconstruction, i.e.,

$$\mathcal{J}_{X:1} = \{\{1\}, \{2\}, \dots, \{K\}\}. \quad (29)$$

1:X This is the reverse of the previous strategy: the input is a single sub-reconstruction, and the target is the mean of the remaining sub-reconstructions, i.e.,

$$\mathcal{J}_{1:X} = \{J^c \mid J \in \mathcal{J}_{X:1}\}. \quad (30)$$

In the 1:X strategy, the input is noisier than the target image, which corresponds to supervised training, where the quality of the target images is usually higher than the input images. The opposite is the case for the X:1 strategy, which corresponds more closely to Noise2Self denoising, where more pixels are used to compute the input than to compute the target images.

Our implementation of Noise2Inverse for tomography is consistent with the theoretical considerations discussed in the previous section. In both strategies, we prevent biasing the reconstructions,

by ensuring that each projection angle occurs in reconstructions at the same rate. In fact, a property of FBP is that the full reconstruction is the mean of the sub-reconstructions. In theory, this means that training converges to the conditional expectation of the *full clean* FBP reconstruction. Furthermore, we use every K th projection angle to compute the reconstructions. This ensures that the reconstructions are homogeneously informative throughout the image, and we prevent “missing wedges”, which occur when adjacent projection angles are used, as in Figure 3. In addition, we use the FBP algorithm with the Ram-Lak filter [1], which does not blur the reconstructions to remove noise. In the next section, we describe the performance of this implementation in practice.

4 Results

We performed several experiments on tomographic reconstruction problems. These experiments were performed with the aim of assessing the performance of the proposed Noise2Inverse method, determining the suitability of Noise2Self denoising for tomographic images, and analyzing the impact of hyper-parameters on the performance of Noise2Inverse.

Comparison to reconstruction techniques Noise2Inverse is compared to conventional tomographic reconstruction algorithms in Sections 4.1 and 4.2. These sections describe a quantitative evaluation on simulated tomographic data and a qualitative evaluation on an existing experimental dataset.

Noise2Self on tomographic images The experiments in Section 4.3 investigate a transfer of Noise2Self denoising to inverse problems. The Noise2Self method was evaluated on two datasets: one dataset with noise common to tomographic reconstructions and one with similar but element-wise independent noise. In addition, Noise2Inverse was compared to several variations of Noise2Self.

Hyper-parameters In Section 4.4, the impact on the reconstruction quality of several variables was investigated, specifically, the number of projection angles N_{θ} , the number of splits K , the training strategy \mathcal{J} , and the neural network architecture.

We first describe the simulated tomographic dataset and our implementation of Noise2Inverse.

Both are used throughout the experiments.

Simulated data A cylindrical foam phantom was generated containing 100,000 randomly-placed non-overlapping bubbles. Analytical projection images of the phantom were computed using the open-source `foam_ct_phantom` package [7]. The value of each detector pixel was calculated by taking the average projection value of four equally-spaced rays through the pixel. Projection images were acquired from 1024 equally spaced angles.

The projection images of the foam dataset were corrupted with various levels of Poisson noise. The noise was varied by altering the average absorption of the sample α and the incident photon count per pixel I_0 . The average absorption of the sample was calculated as the mean of the vector $1 - e^{-\mathbf{y}_i}$ for positions i where \mathbf{y}_i was non-zero, and it was adjusted by modifying the intensity of the sinogram. The pixels in the noisy projections were sampled from \tilde{p} , which for clean pixel value p was distributed as

$$I_0 e^{-\tilde{p}} \sim \text{Poisson}(I_0 e^{-p}).$$

FBP reconstructions were computed on a 512^3 voxel grid with the Ram-Lak filter using the AS-TRA toolbox [18]. On this grid, the radius of the random spheres ranged between 1.5 and 51 voxels. A reconstruction of the central slice of the foam phantom can be found in Figure 4, along with reconstructions of the noisy projection datasets.

Noise2Inverse We describe the Noise2Inverse implementation in terms of neural network architecture and training procedure.

The principal network architecture used throughout the experiments was the mixed-scale dense (MS-D) network [19], of which we used the open-source `msd_pytorch` implementation [20]. The MS-D network has 100 single-channel intermediate layers, and the convolutions in layer i are dilated by $d_i = 1 + (i \bmod 10)$. With 45,652 trainable network parameters, the MS-D architecture has considerably fewer parameters than comparable network architectures, reducing the risk of overfitting to the noise. The MS-D architecture is compared with other architectures in Section 4.4.

The networks were trained for 100 epochs using the ADAM algorithm [21] with a mini-batch size of 12 and a learning rate of 10^{-3} .

4.1 Quantitative comparison

In this section, Noise2Inverse is compared to two conventional iterative reconstruction techniques: the simultaneous iterative reconstruction technique (SIRT) [22] and Total-Variation Minimization (TV-MIN) [23]. The reconstruction quality of these methods is assessed on a simulated foam phantom dataset with various noise profiles.

For Noise2Inverse, we used the X:1 training strategy with $K = 4$ splits. We show that this is a robust choice in Section 4.4.

Iterative reconstruction The hyper-parameters of SIRT and TV-MIN were tuned using the usually unavailable clean reconstructions. Therefore, the results of SIRT and TV-MIN might be better than what is achievable in practice, but they serve as a useful reference for comparison to Noise2Inverse. SIRT has no explicit hyper-parameters, but its iterative nature can be exploited for regularization: early stopping of the algorithm can attenuate high-frequency noise in the reconstructed image [22]. We selected the number of iterations (with a maximum of 1000) with the lowest Peak Signal to Noise Ratio (PSNR) on the central slice with respect to the clean reconstruction.

The FISTA algorithm [23] was used to calculate the TV-MIN reconstruction. TV-MIN has a regularization parameter λ that effectively penalizes steps in the gray value of the reconstructed image. As with SIRT, we selected the optimal number of iterations (with a maximum of 500) based on the PSNR of the central slice with respect to the clean reconstruction, and the optimal value of the λ parameter was determined using the Nelder-Mead method [24].

Metrics and evaluation The output of each method was compared to the clean FBP reconstruction using two metrics: the structural similarity index (SSIM) [25] and the Peak Signal to Noise Ratio (PSNR). Because the reconstructed images did not fall in the $[0, 1]$ range, these metrics were computed with a data range that was determined by the minimum and maximum intensity of the clean reconstructed images.

The top row of Figure 5 displays the output of Noise2Inverse for the central slice of the three simulated datasets. Denoising these datasets is challenging, as can be seen when comparing with SIRT

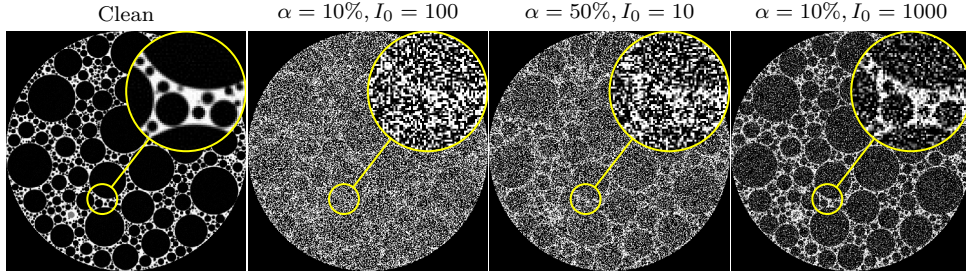


Figure 4: Displays of the clean reconstruction (left) and low-dose reconstructions of the central slice of the foam phantom. Both α , the absorption of the phantom and I_0 , the initial photon count per pixel, were varied. The yellow insets show an enlarged view of the reconstructions.

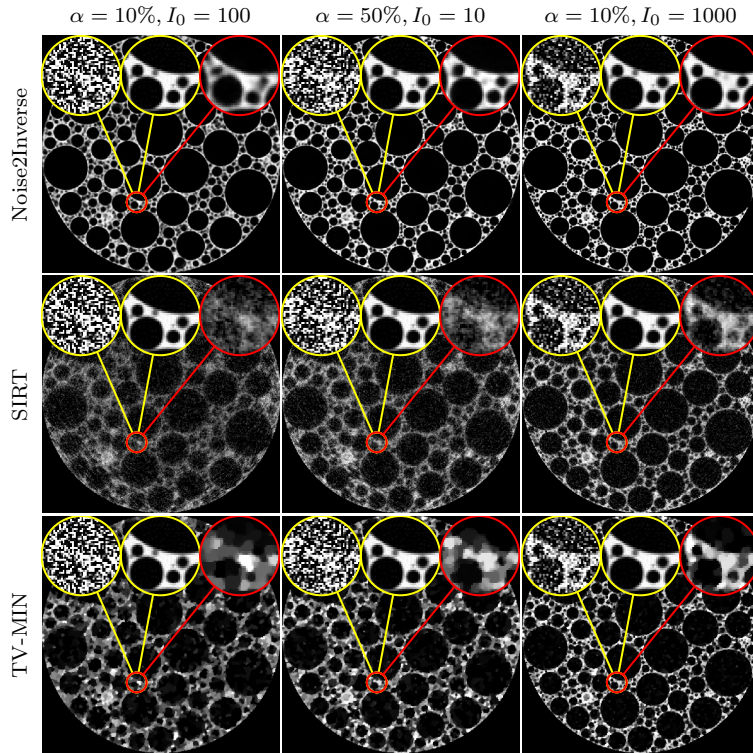


Figure 5: Results of Noise2Inverse, SIRT, and TV-MIN on simulated foam phantoms with varying absorption α and photon count I_0 . Results are shown on the central slice. The insets display the noisy and clean reconstructions (yellow) and the algorithm output (red).

Table 1: Comparison of PSNR and SSIM metrics for SIRT, TV-MIN, and Noise2Inverse at several noise profiles with varying absorption α and incident photon count I_0 .

α	I_0	Method	PSNR	SSIM
10%	100	Noise2Inverse	19.71	0.78
		TV-MIN	16.89	0.46
		SIRT	15.56	0.36
50%	10	Noise2Inverse	21.66	0.79
		TV-MIN	18.08	0.53
		SIRT	16.53	0.42
10%	1000	Noise2Inverse	26.25	0.89
		TV-MIN	21.24	0.68
		SIRT	18.84	0.53

and TV-MIN: these algorithms fail to recover several fine details. In contrast, our method achieves a much improved visual impression on all three datasets. As can be seen in Table 1, the PSNR and SSIM metrics of the Noise2Inverse method are considerably higher.

4.2 Qualitative comparison: experimental data

The Noise2Inverse method was compared to SIRT and TV-MIN on an existing real-world experimental dataset from TomoBank [26]. The dataset, `Dorthe_F_002`, was acquired at the Advanced Photon Source at Argonne National Laboratory, and contained 900 noisy projection images of 960×600 pixels depicting a cylinder of glass beads that was scanned at experimental conditions designed to capture the dynamics of fast evolving samples. At 6 milliseconds per projection image, the exposure time was therefore much shorter than what is required for low-noise data acquisition [26]. The data was pre-processed with the TomoPy software package [27] and reconstructed with FBP [18], resulting in 900 2D slices of 960×960 pixels. We stress that no low-noise projection images were available.

For Noise2Inverse, an MS-D network was trained with the X:1 strategy and 4 splits for 100 epochs. The best parameter settings for SIRT and TV-MIN were determined by visual inspection. For SIRT, the best reconstruction was chosen from 1000 iter-

ations on the central slice. For TV-MIN, the number of iterations was fixed at 500, and the optimal value of the regularization parameter was chosen from $2^{-30}, 2^{-29}, \dots, 2^{-10}$. After initial reconstructions, we found that the reported value of the center of rotation offset — 4.5 pixels from center — yielded unsatisfactory results. The reconstructions in Figure 6 were computed with a center of rotation that was shifted by 8.9 pixels. Results are shown for the central slice of the reconstructed volume. The FBP and SIRT reconstructions exhibit severe noise. The TV-MIN reconstruction improves on the level of noise, but contains stepping artifacts that reduce the effective resolution. Our method is able to remove the noise while retaining the finer structure of the image.

4.3 Self-supervised image denoising for tomography

The performance of Noise2Self on tomographic images was evaluated in two experiments. The first experiment tested the element-wise independence requirement, by evaluating Noise2Self on images corrupted by element-wise independent noise and on images reconstructed from noisy projection data. The second experiment was a comparison of Noise2Inverse to Noise2Self, including variations of Noise2Self applied to projection and sinogram images. We first describe the Noise2Self implementation.

Noise2Self The original implementation of Noise2Self [14] was used, which obtains better performance than the simplified scheme discussed in Section 2.1. The training procedure was the same as for Noise2Inverse: an MS-D network was trained for 100 epochs as described at the beginning of Section 4.

Tomographic versus photographic noise Noise2Self was applied to images with noise common to CT and to similar but element-wise independent noise. In these experiments, the same foam phantom was used as before, and Gaussian noise was used throughout the comparison to strictly compare the independence properties of the noise. First, we confirmed that Noise2Self obtained denoised images when the noise satisfied the element-wise independence property. In this first case, a clean reconstruction was computed on a 512^3 voxel grid, and independent and identically distributed

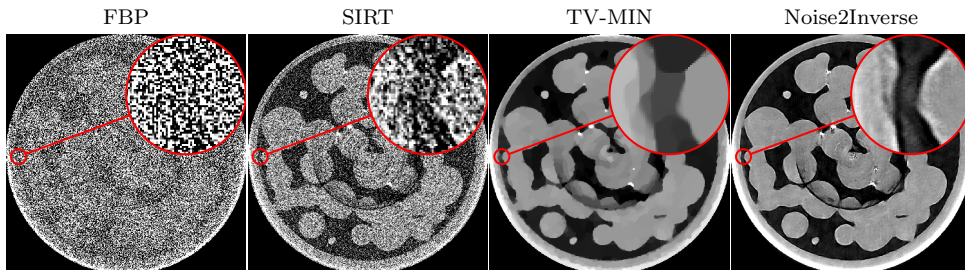


Figure 6: Reconstructions of cylinder containing glass beads [26] using: FBP, SIRT, TV-MIN, and the proposed Noise2Inverse method. The red insets show an enlarged view of the algorithm output.

(i.i.d.) Gaussian noise was added to the reconstructed images. The PSNR of the noisy volume with respect to the clean reconstruction was 11.06. Then, Noise2Self was applied to obtain a denoised volume with significantly improved PSNR of 25.23. This process is displayed in the top row of Figure 7.

Next, we investigated how Noise2Self performed on coupled noise common to CT. In this case, i.i.d. Gaussian noise was added to the projection images, and a reconstruction was computed afterwards. The PSNR of this noisy reconstruction with respect to the clean reconstruction was 11.59. When Noise2Self was applied to the noisy reconstructed volume, it obtained a PSNR of 16.14, which is only half of the improvement that it obtained in the first case. This process is displayed in the bottom row of Figure 7.

The results displayed in Figure 7 demonstrate that the performance of Noise2Self is substantially degraded when the noise is not element-wise independent. Even though the starting PSNR in the bottom row is slightly higher, the PSNR improvement is only half of the top row. In the top row, the validation error continued to improve for 100 epochs, whereas in the bottom row, training started to overfit to the noise within the first 10 epochs of training, which could be caused by the statistical dependence between the input and target images.

Noise2Self on sinogram and projections To mitigate the effect of coupled noise, Noise2Self was also applied to images that do satisfy the pixel-wise independence property: the projection images and sinograms. In these cases, Noise2Self was first applied to denoise the raw images, and reconstructions were computed from the denoised projection images or sinograms.

Table 2: Comparison of PSNR and SSIM metrics for Noise2Self on reconstruction, projection, and sinogram images.

α	I_0	Method	PSNR	SSIM
10%	100	N2S Reconstructions	6.37	0.27
		N2S Projections	16.43	0.44
		N2S Sinograms	<i>16.98</i>	<i>0.45</i>
		Noise2Inverse	19.71	0.78
50%	10	N2S Reconstructions	9.12	0.20
		N2S Projections	17.49	0.49
		N2S Sinograms	<i>18.06</i>	<i>0.51</i>
		Noise2Inverse	21.66	0.79
10%	1000	N2S Reconstructions	15.39	0.50
		N2S Projections	19.57	<i>0.62</i>
		N2S Sinograms	<i>20.62</i>	0.60
		Noise2Inverse	26.25	0.89

As can be seen in Figure 8, the variations of Noise2Self did improve results, but not beyond Noise2Inverse. Although applying Noise2Self on the projection and sinogram images did accurately denoise the raw images, the resulting reconstructions of these denoised images exhibited some blurring (projections) and streaks (sinograms). As displayed in Table 2, the Noise2Self-based method with the best metrics, Noise2Self on sinograms, obtains PSNR on par with TV-MIN and SSIM worse than TV-MIN, see Table 1.

4.4 Hyper-parameters

We analyzed the influence of the number of splits, training strategy, number of projection angles, and

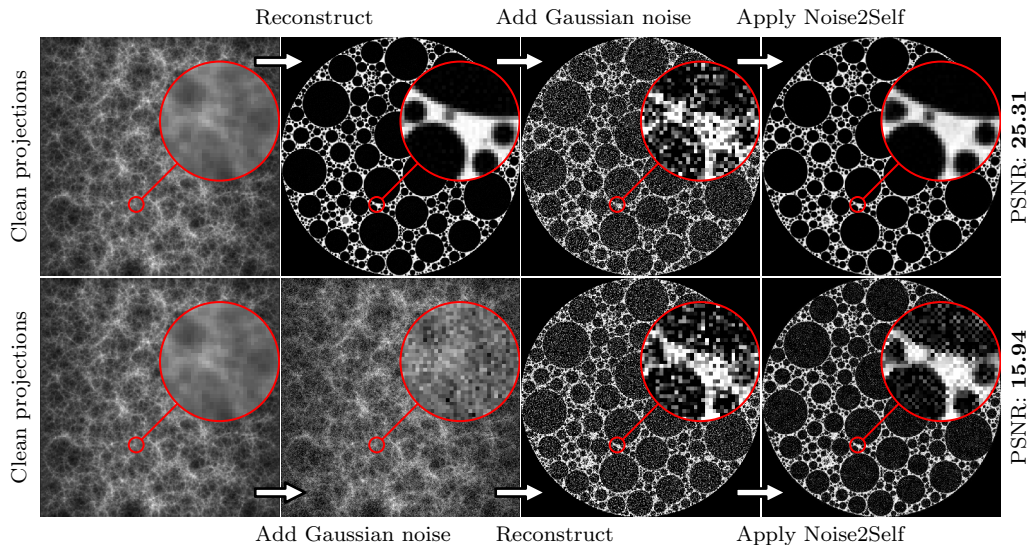


Figure 7: The effect of element-wise independence of the noise on the Noise2Self method. In the top row, Gaussian noise is added to a reconstruction, and Noise2Self is applied to remove it. In the bottom row, Gaussian noise is added to the projections before reconstruction, resulting in a reconstructed image with similar but coupled noise. Noise2Self achieves lower PSNR in the bottom row than in the top row.

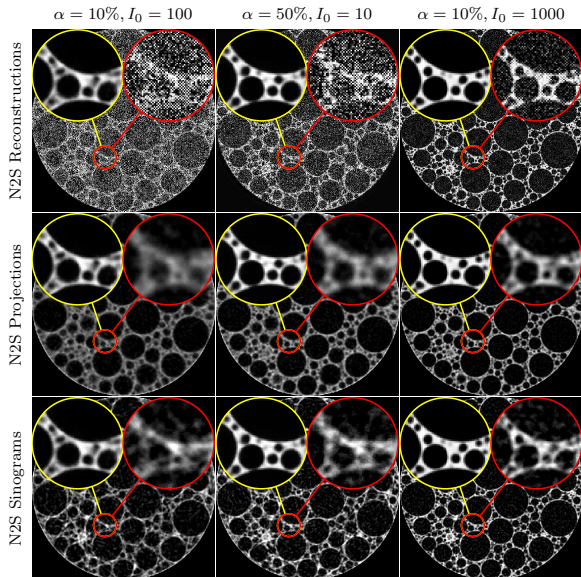


Figure 8: From top to bottom, results on the central slice of the foam phantom of Noise2Self applied to reconstructed, projection, and sinogram images. For comparison, the insets show the output of Noise2Inverse (yellow) and Noise2Self (red).

neural network architecture on the effectiveness of Noise2Inverse.

The same foam phantom was used, and noisy projection data were acquired from 512, 1024, and 2048 angles, of which the first and last acquisitions were under-sampling and over-sampling the projection angles, respectively. For each dataset, the total number of incident photons remained constant: we used $I_0 = 400, 200, 100$ for $N_\theta = 512, 1024, 2048$, respectively. The average absorption was 23%, which is the default value of the `foam_ct_phantom` package.

Splits and strategy The performance of the Noise2Inverse method was evaluated with a number of splits $K = 2, 4, 8, 16, 32$, and with strategies X:1 and 1:X, see Equations (29) and (30). These experiments were performed with MS-D networks, which were trained for 100 epochs, and used the same training procedure as before.

The PSNR metrics are displayed in Figure 9. The figure shows that the X:1 strategy yields considerably better results than the 1:X strategy, except for $K = 2$, where they are equivalent. Setting the number of splits to $K = 2$ yields good results across the board, but the PSNR can be improved

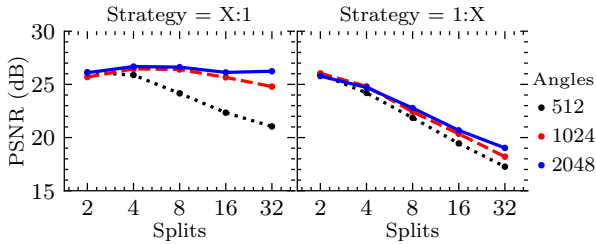


Figure 9: The PSNR metric for the Noise2Inverse method with the MS-D network applied on the foam phantom with varying number of splits, angles, and varying input-target splitting strategies. The X:1 strategy attains higher PSNR than the 1:X strategy.

by setting K to 4 or 8, if the projection angles are not under-sampled. In general, the figure shows that increasing the number of acquired projection images can improve reconstruction quality without increasing the photon count.

Neural network architectures We compared three neural network architectures: the U-Net [28], DnCNN [15], and the previously described MS-D [19] network architectures, all of which were implemented in PyTorch [29].

The U-net is based on a widely available open source implementation¹, which is a mix of the architectures described in [28, 30]. Like [28], the images are down-sampled four times using 2×2 max-pooling, the “up-convolutions” have trainable parameters, and the convolutions have 3×3 kernels. Like [30], this implementation uses batch normalization before each ReLU, the smallest image layers are 512 channels instead of 1024 channels, and zero-padding is used instead of reflection-padding. The resulting network has 14,787,777 trainable network parameters.

We used the DnCNN implementation from [14] with a depth of 20 layers, which is advised for non-Gaussian denoising [15]. The resulting network has 667,008 trainable network parameters.

The previous experiment was repeated on the dataset containing 1024 projection images. The networks were trained for 100 epochs, and used the same training procedure as before. The results are displayed in Figure 10. The figure shows that the U-net achieved overall highest performance using

¹<https://github.com/milesial/Pytorch-UNet/>

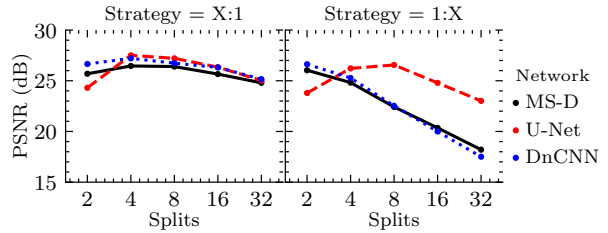


Figure 10: Comparison of the PSNR metric. The MS-D, U-Net, and DnCNN networks were trained for 100 epochs on the foam phantom with 1024 projection angles.

the X:1 strategy with 4 splits. In addition, the effect of the number of splits K is roughly the same across strategies and network architectures, except for U-net. In fact, the PSNR metric of the U-Net with the 1:X strategy initially increases when K is increased, which might be due to the large network architecture and number of parameters compared to the other two neural network architectures. Nonetheless, the X:1 strategy consistently attains higher PSNR than the 1:X for the U-net as well. We note that the U-Nets performed worse than the other networks with 2 splits, which suggests that training might have overfit the noise.

Overfitting We tested if the networks overfit the noise when trained for a long time. All three networks were trained for 1000 epochs using the X:1 strategy and $K = 4$ on the same foam dataset with 1024 projection angles. The resulting PSNR on the central slice as training progressed is displayed in Figure 11. The figure shows that U-Net and DnCNN started to fit the noise, whereas the PSNR of the MS-D network continued to increase. This matches earlier results on overfitting [19, 31].

5 Discussion

The results show that the proposed Noise2Inverse method outperforms conventional reconstruction algorithms SIRT and TV-MIN by a large margin as measured in PSNR and SSIM. This improvement is accomplished despite optimizing the hyper-parameters of SIRT and TV-MIN on the clean reconstruction and without likewise optimizing the Noise2Inverse hyper-parameters. In addition, Noise2Inverse is able to significantly reduce

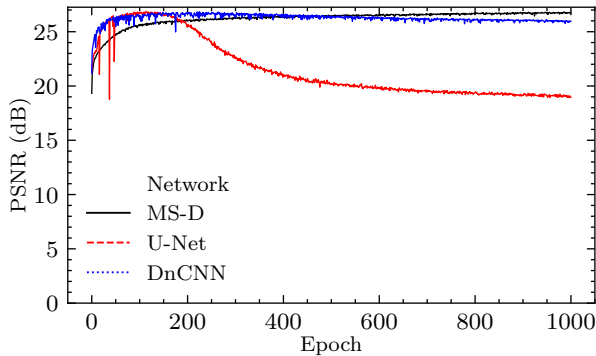


Figure 11: The PSNR on the central slice as training progressed. A U-Net, DnCNN, and MS-D network were trained with the X:1 strategy and number of splits $K = 4$ for 1000 epochs on the foam phantom reconstructed from 1024 projection angles.

noise in challenging real-world experimental data, improving on the visual impression obtained by SIRT and TV-MIN.

Extending the Noise2Self framework [14], we describe a general framework for denoising in linear inverse problems in imaging that provides a theoretical rationale for the success of our method. The framework shows that clean reconstructions may be recovered from noisy measurements *without observing clean measurements*, under the common assumption that the measured noise is element-wise independent and mean-zero.

The framework points the way to new applications of Noise2Inverse in linear inverse problems in imaging. The implementation of Noise2Inverse for tomography shows that several aspects are worth considering. If reconstruction artifacts arise in the absence of noise, they will be preserved. In addition, if the reconstruction algorithm filters the noise at the expense of resolution, this will cause blurring in the output of our method. Moreover, splitting the measurement uniformly can avoid biasing the output of the method towards a particular subset of the measured data. Finally, the performance of the neural network can be improved by ensuring that the sub-reconstructions are homogeneously informative throughout the image. Taking into account these considerations, we expect that our method can be effectively applied to linear inverse problems

in imaging other than tomography.

The comparison of Noise2Inverse with Noise2Self demonstrates that the success of our method depends not only on considerations of statistical independence, but also on taking account of the physical forward model. Regarding statistical independence, we have demonstrated that a straightforward application of Noise2Self fails on noisy tomographic reconstructions due to coupling of the noise. Regarding the forward model, we have investigated a two-step approach, where Noise2Self is applied to projection or sinogram images — which *do* satisfy the element-wise independence requirement — before reconstructing. This approach performs worse than TV-MIN and Noise2Inverse in terms of visual impression and quality metrics. This matches earlier results [10], and could result from the fact that the consistency of the projection and sinogram images with respect to the forward operator is not necessarily preserved. These results suggest that taking into account the properties of the inverse problem — as Noise2Inverse does — significantly improves the quality of the reconstruction.

Several variables affect the performance of Noise2Inverse. Most importantly, the training strategy that reconstructs the input images from at least as many projection angles as the target images — the X:1 strategy — yields better results than vice versa. This conclusion holds regardless of network architecture, number of splits, or number of projection angles. This suggests that noise in the gradient is less problematic than noise in the input for neural network training, as was observed before [12]. Another variable that consistently predicts performance is the number of angles; acquiring more projections yields a small but consistent performance boost. The number of parts in which the measured data is split, however, deserves more nuance: when the projection angles are under-sampled, the results indicate that two parts yield the best results; otherwise, splitting into more parts yields better results. Finally, maximal performance can be obtained by tuning the neural network architecture and number of training iterations. When tuning is not an option, an MS-D network can be trained with limited risk of overfitting the noise.

6 Conclusion

We have proposed Noise2Inverse, a CNN-based method for denoising linear inverse problems in imaging that does not require any additional clean or noisy data beyond the acquired noisy dataset. On tomographic reconstruction problems, it strongly outperforms both standard reconstruction techniques such as Total-Variation Minimization, and self-supervised image denoising-based techniques, such as Noise2Self. We also demonstrate that the method is able to significantly reduce noise in challenging real-world experimental datasets. Finally, our general framework paves the way for applications to linear inverse problems in imaging other than tomography.

Appendix

Proof. [of Proposition 1] First, expand the squared norm [32, Lemma 3.12]

$$\begin{aligned} \|h(\tilde{x}_{J^c}) - \tilde{x}_J\|^2 &= \|h(\tilde{x}_{J^c}) - x^*_{J^c} + x^*_{J^c} - \tilde{x}_J\|^2 \\ &= \|h(\tilde{x}_{J^c}) - x^*_{J^c}\|^2 + \|x^*_{J^c} - \tilde{x}_J\|^2 \\ &\quad + 2\langle h(\tilde{x}_{J^c}) - x^*_{J^c}, x^*_{J^c} - \tilde{x}_J \rangle. \end{aligned}$$

Let $x \in \mathcal{X}$, $y = \mathbf{A}x$, and $J \in \mathcal{J}$. Then, from Equation (17), we obtain

$$\begin{aligned} \mathbb{E}_\mu [\tilde{x}_J | x, J] &= \mathbb{E}_\mu [\mathbf{R}_J \tilde{y}_J | x, J] \\ &= \mathbf{R}_J \mathbb{E}_{x, \epsilon} [y_J + \epsilon_J | x] \\ &= \mathbf{R}_J y_J \\ &= x^*_J, \end{aligned} \tag{31}$$

where we use that \mathbf{R}_J is linear.

The noisy random variables \tilde{x}_{J^c} and \tilde{x}_J are independent conditioned on x and J , since domains of \mathbf{R}_J and \mathbf{R}_{J^c} do not overlap, and the noise ϵ is element-wise statistically independent. This independence condition allows us to interchange the order of the expectation and inner product [33, Proposition 2.3], which yields, using Equation (31),

$$\begin{aligned} &\mathbb{E} [\langle h(\tilde{x}_{J^c}) - x^*_{J^c}, x^*_{J^c} - \tilde{x}_J \rangle | x, J] \\ &= \langle \mathbb{E} [h(\tilde{x}_{J^c}) - x^*_{J^c} | x, J], \mathbb{E} [x^*_{J^c} - \tilde{x}_J | x, J] \rangle \\ &= \langle \mathbb{E} [h(\tilde{x}_{J^c}) - x^*_{J^c} | x, J], 0 \rangle \\ &= 0. \end{aligned}$$

Using the tower property of expectation, we obtain

$$\begin{aligned} &\mathbb{E}_\mu \|h(\tilde{x}_{J^c}) - \tilde{x}_J\|^2 \\ &= \mathbb{E} \left[\mathbb{E} [\|h(\tilde{x}_{J^c}) - \tilde{x}_J\|^2 | x, J] \right] \\ &= \mathbb{E} \left[\mathbb{E} [\|h(\tilde{x}_{J^c}) - x^*_{J^c}\|^2 + \|x^*_{J^c} - \tilde{x}_J\|^2 | x, J] \right] \\ &= \mathbb{E}_\mu \|h(\tilde{x}_{J^c}) - x^*_{J^c}\|^2 + \mathbb{E}_\mu \|x^*_{J^c} - \tilde{x}_J\|^2. \end{aligned}$$

□

Similar proofs can be found in [14, 17].

Acknowledgment

The authors acknowledge financial support from the Dutch Research Council (NWO), project numbers 639.073.506 and 016.Veni.192.235. The authors have made use of the following additional software packages to compute and visualize the experiments: Snakemake, Sacred, Matplotlib, pandas, and scikit-image [34–38].

References

- [1] Thorsten M. Buzug. *Computed Tomography : from Photon Statistics to Modern Cone-Beam CT*. Springer, 2008.
- [2] G. A. Wright. Magnetic resonance imaging. *IEEE Signal Processing Magazine*, 14(1):56–66, 1997.
- [3] R. G. Ellis and D. W. Oldenburg. Applied geophysical inversion. *Geophysical Journal International*, 116(1):5–11, 1994.
- [4] Chinmay Belthangady and Loic A. Royer. Applications, promises, and pitfalls of deep learning for fluorescence image reconstruction. *Nature Methods*, 16(12):1215–1225, 2019.
- [5] Eunhee Kang, Junhong Min, and Jong Chul Ye. A deep convolutional neural network using directional wavelets for low-dose X-ray CT reconstruction. *Medical Physics*, 44(10):e360–e375, 2017.

- [6] Cynthia H. McCollough, Adam C. Bartley, Rickey E. Carter, Baiyu Chen, Tammy A. Drees, Phillip Edwards, David R. Holmes, Alice E. Huang, Farhana Khan, Shuai Leng, and et al. Low-dose CT for the detection and classification of metastatic liver lesions: Results of the 2016 low dose CT grand challenge. *Medical Physics*, 44(10):e339–e352, 2017.
- [7] Daniël M. Pelt, Kees Joost Batenburg, and James A. Sethian. Improving tomographic reconstruction from limited data using mixed-scale dense convolutional neural networks. *Journal of Imaging*, 4(11):128, 2018.
- [8] Yu Sun, Zhihao Xia, and Ulugbek S. Kamilov. Efficient and accurate inversion of multiple scattering with deep learning. *Optics Express*, 26(11):14678, 2018.
- [9] Won Chang, Jeong Min Lee, Kyunghye Lee, Jeong Hee Yoon, Mi Hye Yu, Joon Koo Han, and Byung Ihn Choi. Assessment of a model-based, iterative reconstruction algorithm (MBIR) regarding image quality and dose reduction in liver computed tomography. *Investigative Radiology*, 48(8):598–606, 2013.
- [10] Tim-Oliver Buchholz, Mareike Jordan, Gaia Pigino, and Florian Jug. Cryo-care: Content-aware image restoration for cryo-transmission electron microscopy data. *2019 IEEE 16th International Symposium on Biomedical Imaging (ISBI 2019)*, 2019.
- [11] Shakarim Soltanayev and Se Young Chun. Training deep learning based denoisers without ground truth data. In *Advances in Neural Information Processing Systems 31*, pages 3261–3271. Curran Associates, Inc., 2018.
- [12] Jaakko Lehtinen, Jacob Munkberg, Jon Hasselgren, Samuli Laine, Tero Karras, Miika Aittala, and Timo Aila. Noise2Noise: Learning image restoration without clean data. In *Proceedings of the 35th International Conference on Machine Learning*, volume 80, pages 2965–2974. PMLR, 2018.
- [13] Alexander Krull, Tim-Oliver Buchholz, and Florian Jug. Noise2Void - learning denoising from single noisy images. In *The IEEE Conference on Computer Vision and Pattern Recognition (CVPR)*, June 2019.
- [14] Joshua Batson and Loic Royer. Noise2Self: Blind denoising by self-supervision. In *Proceedings of the 36th International Conference on Machine Learning*, volume 97, pages 524–533. PMLR, 2019.
- [15] Kai Zhang, Wangmeng Zuo, Yunjin Chen, Deyu Meng, and Lei Zhang. Beyond a gaussian denoiser: Residual learning of deep CNN for image denoising. *IEEE Transactions on Image Processing*, 26(7):3142–3155, 2017.
- [16] K. Dabov, A. Foi, V. Katkovnik, and K. Egiazarian. Image denoising by sparse 3-D transform-domain collaborative filtering. *IEEE Transactions on Image Processing*, 16(8):2080–2095, 2007.
- [17] Jonas Adler and Ozan Öktem. Deep bayesian inversion. *CoRR*, 2018.
- [18] Wim van Aarle, Willem Jan Palenstijn, Jan De Beenhouwer, Thomas Altantzis, Sara Bals, K. Joost Batenburg, and Jan Sijbers. The ASTRA toolbox: a platform for advanced algorithm development in electron tomography. *Ultramicroscopy*, 157:35–47, 2015.
- [19] Daniël M. Pelt and James A. Sethian. A mixed-scale dense convolutional neural network for image analysis. *Proceedings of the National Academy of Sciences*, 115(2):254–259, 2017.
- [20] Allard Hendriksen. ahendriksen/msd_pytorch: v0.7.2, December 2019.
- [21] Diederik P. Kingma and Jimmy Ba. ADAM: A method for stochastic optimization. In *Proceedings of the 3rd International Conference on Learning Representations*, 2014.
- [22] Jens Gregor and Thomas Benson. Computational analysis and improvement of SIRT. *IEEE Transactions on Medical Imaging*, 27(7):918–924, 2008.

- [23] A. Beck and M. Teboulle. Fast gradient-based algorithms for constrained total variation image denoising and deblurring problems. *IEEE Transactions on Image Processing*, 18(11):2419–2434, 2009.
- [24] Pauli Virtanen, Ralf Gommers, Travis E. Oliphant, Matt Haberland, Tyler Reddy, David Cournapeau, Evgeni Burovski, Pearu Peterson, Warren Weckesser, Jonathan Bright, Stéfan J. van der Walt, Matthew Brett, Joshua Wilson, K. Jarrod Millman, Nikolay Mayorov, Andrew R. J. Nelson, Eric Jones, Robert Kern, Eric Larson, CJ Carey, İlhan Polat, Yu Feng, Eric W. Moore, Jake VanderPlas, Denis Laxalde, Josef Perktold, Robert Cimrman, Ian Henriksen, E. A. Quintero, Charles R Harris, Anne M. Archibald, Antônio H. Ribeiro, Fabian Pedregosa, Paul van Mulbregt, and SciPy 1.0 Contributors. SciPy 1.0—fundamental Algorithms for Scientific Computing in Python. *arXiv e-prints*, page arXiv:1907.10121, 2019.
- [25] Z. Wang, A.C. Bovik, H.R. Sheikh, and E.P. Simoncelli. Image quality assessment: From error visibility to structural similarity. *IEEE Transactions on Image Processing*, 13(4):600–612, 2004.
- [26] Francesco De Carlo, Doğa Gürsoy, Daniel J Ching, K Joost Batenburg, Wolfgang Ludwig, Lucia Mancini, Federica Marone, Rajmund Mokso, Daniël M Pelt, Jan Sijbers, and et al. TomoBank: a tomographic data repository for computational X-ray science. *Measurement Science and Technology*, 29(3):034004, 2018.
- [27] Doğa Gürsoy, Francesco De Carlo, Xianghui Xiao, and Chris Jacobsen. Tomopy: a framework for the analysis of synchrotron tomographic data. *Journal of Synchrotron Radiation*, 21(5):1188–1193, 2014.
- [28] Olaf Ronneberger, Philipp Fischer, and Thomas Brox. U-Net: Convolutional networks for biomedical image segmentation. *Medical Image Computing and Computer-Assisted Intervention - MICCAI 2015*, pages 234–241, 2015.
- [29] Adam Paszke, Sam Gross, Soumith Chintala, Gregory Chanan, Edward Yang, Zachary DeVito, Zeming Lin, Alban Desmaison, Luca Antiga, and Adam Lerer. Automatic differentiation in PyTorch. In *NIPS-W*, 2017.
- [30] Özgün Çiçek, Ahmed Abdulkadir, Soeren S. Lienkamp, Thomas Brox, and Olaf Ronneberger. 3D U-Net: Learning dense volumetric segmentation from sparse annotation. *Lecture Notes in Computer Science*, pages 424–432, 2016.
- [31] Allard A. Hendriksen, Daniël M. Pelt, Willem Jan Palenstijn, Sophia B. Coban, and Kees Joost Batenburg. On-the-fly machine learning for improving image resolution in tomography. *Applied Sciences*, 9(12), 2019.
- [32] Bryan P. Rynne and Martin A. Youngson. Linear functional analysis. *Springer Undergraduate Mathematics Series*, 2008.
- [33] Morris L. Eaton. *Chapter 2, Random Vectors*, volume Volume 53 of *Lecture Notes—Monograph Series*, pages 70–102. Institute of Mathematical Statistics, 2007.
- [34] J. Koster and S. Rahmann. Snakemake—a scalable bioinformatics workflow engine. *Bioinformatics*, 28(19):2520–2522, 2012.
- [35] Klaus Greff, Aaron Klein, Martin Chovanec, Frank Hutter, and Jürgen Schmidhuber. The Sacred infrastructure for computational research. *Proceedings of the 16th Python in Science Conference*, 2017.
- [36] Wes McKinney. Pandas: a foundational Python library for data analysis and statistics. *Python for High Performance and Scientific Computing*, 14, 2011.
- [37] John D. Hunter. Matplotlib: a 2D graphics environment. *Computing in Science & Engineering*, 9(3):90–95, 2007.
- [38] Stéfan van der Walt, Johannes L. Schönberger, Juan Nunez-Iglesias, François Boulogne, Joshua D. Warner, Neil Yager, Emmanuelle Guillard, and Tony Yu. Scikit-image: Image processing in Python. *PeerJ*, 2:e453, 2014.